Micron-scale ballistic thermal conduction and suppressed thermal conductivity in heterogeneously interfaced nanowires

Tzu-Kan Hsiao (蕭子綱),[1,2] Bor-Woei Huang (黃柏瑋),[1] Hsu-Kai Chang (張旭凱),[3] Sz-Chian Liou (劉思謙),[1]
Ming-Wen Chu (朱明文),[1] Si-Chen Lee (李嗣涔),[3] and Chih-Wei Chang (張之威)[1,*]

[1]*Center for Condensed Matter Sciences, National Taiwan University, Taipei 10617, Taiwan*
[2]*Institute of Applied Physics, National Taiwan University, Taipei 10617, Taiwan*
[3]*Graduate Institute of Electronic Engineering, National Taiwan University, Taipei 10617, Taiwan*

By employing three different measurement methods, we rigorously show that micron-scale ballistic thermal conduction can be found in Si-Ge heterogeneously interfaced nanowires exhibiting low thermal conductivities. The heterogeneous interfaces localize most high-frequency phonons and suppress the total thermal conductivity below that of Si or Ge. Remarkably, the suppressed thermal conductivity is accompanied with an elongation of phonon mean free paths over 5 μm at room temperature, which is not only more than 25 times longer than that of Si or Ge but also longer than those of the best thermal conductors like diamond or graphene. We estimate that only 0.1% of the excited phonons carry out the heat transfer process, and, unlike phonon transport in Si or Ge, the low-frequency phonons in Si-Ge core-shell nanowires are found to be insensitive to twin boundaries, defects, and local strain. The ballistic thermal conduction persisting over 5 μm, along with the suppressed thermal conductivity, will enable wave engineering of phonons at room temperature and inspire new improvements of thermoelectric devices.

I. INTRODUCTION

Intuitively, the analogy of phonon transport to electron transport seems to suggest that high thermal conductivity materials would be ballistic thermal conductors with a long phonon mean free path (l); the best thermal conductors, like nanotubes, graphene, and diamond, are known to exhibit a long l (∼1 μm) at room temperature [1,2]. However, because phonons of a wide range of frequencies may contribute to the heat conduction in general, the intuitive analogy does not fully capture the nature of phonon transport. In fact, the key difference between electron transport and phonon transport can be seen from the formulation

$$\kappa = \frac{1}{3} \sum_n C_n v_n l_n, \tag{1}$$

where κ is thermal conductivity, C_n is the volumetric specific heat, v_n is the averaged phonon velocity, and l_n is the phonon mean free path of the nth phonon mode. Notably, the sum over all excited phonon modes is shown in Eq. (1), whereas it is absent in the Drude model, denoting the fundamental difference between electrical and thermal transport phenomena.

Unfortunately, the general scale of $l < 100$ nm for most materials has made experimental findings of ballistic thermal conduction extremely difficult, especially at room temperature. Although recent time-domain thermoreflectance measurements indicate that micron-long l_ns may dominate the heat transfer of Si [3–5], ballistic thermal conduction was not found in conventional thermal transport experiments on samples of similar sizes [6,7]. The fundamental limitation of short ls of most materials has impeded the technological progress of wave engineering of phonons at room temperature [8].

Recently it was found that surprisingly long ls can be found in homogeneously alloyed SiGe nanowires [9]. It is shown that alloy concentrations as low as 10% are sufficient for localizing most high frequency phonons and realizing ballistic thermal conduction over 8.3 μm at room temperature. However, it is unclear how the phonon filtering mechanism sets in when alloying a small amount of Ge into pure Si. Notably, pure Si and Ge exhibit high κs ($\kappa_{Si} = 150$ W/m-K, $\kappa_{Ge} = 58$ W/m-K) but short ls ($l_{Si} < 140$ nm, $l_{Ge} < 100$ nm), whereas SiGe exhibits low κ (<10 W/m-K) but long l (>8.3 μm) [9]. The comparison makes the investigation of the phonon filtering mechanism particularly intriguing.

Si-Ge core-shell nanowires are heterogeneously alloyed materials with tubular-structured interfaces. It is suggested that they exhibit many interesting heat transfer phenomena, including enhanced interface phonon scatterings and phonon localization induced by surface coating [10–15]. Experimentally, recent papers on Ge-Si core-shell nanowires or on homogeneously alloyed SiGe nanowires reporting unexpected suppression of κ have made the topic particularly interesting [9,16–19]. Here we provide evidence from three independent experimental methods that the suppression of κ in Si-Ge core-shell nanowires is in fact accompanied by an unexpected elongation of phonon mean free path over 5 μm, which is much longer than those of the best thermal conductors such as diamond or graphene. Our result not only disentangles the misconception between high κ and long l, but it also points out that the heterogeneous interfaces can induce phonon filtering in the body of a Si-Ge core-shell nanowire. Even if interlayer diffusion occurs across the Si-Ge boundaries, alloy concentrations less than 5% are sufficient to induce the phonon filtering. The mechanism enables low frequency phonons, which occupy ∼0.1% of the excited phonon spectra, to become the dominant heat carriers of the material.

_____
*cwchang137@ntu.edu.tw

II. EXPERIMENTS

A. Nanowire synthesis and characterization

The heterogeneously interfaced SiGe core-shell nanowires were synthesized in a quartz tube furnace by a chemical vapor deposition method [20,21]. Au nanoparticles in colloid solution were first dripped on cleaned silicon wafers before they were loaded into the deposition system. SiH$_4$ (10% diluted in N$_2$) and GeH$_4$ (10% diluted in N$_2$) were used as the precursor gases to initiate the growth. During the heating period, the reaction chamber was repeatedly purged with N$_2$. The growth was set at 445°C. The total pressure was kept at 30 torr during the growth. The flow rates of SiH$_4$ and GeH$_4$ were set at 24 to 40 sccm.

The structures of the synthesized nanowires were characterized by transmission electron microscopy (TEM). Because the intensity of the high-angle annular dark field (HAADF) images obtained in a scanning TEM (STEM) is approximately proportional to $Z^{1.7}$ (Z is the atomic number), the contrast of the image shown in Fig. 1(a) demonstrates that the nanowire exhibits heavy atoms (Ge) in the shell and light atoms (Si) in the core. Further spatially resolved energy dispersive x-ray spectroscopy (EDS) spectra in Fig. 1(b) and STEM-EDS spectral imaging across the nanowire in Figs. 1(c)–1(e) reaffirm the presence of Si in the core region and Ge in the shell region. As shown in Figs. 1(c)–1(e), the absence of Ge/Si signals in the core/shell puts an upper limit of alloy concentration as less than 5% in either region.

B. Method I

To determine l of the nanowire, we note that the definition of l represents a characteristic distance beyond which the phonon transport transits from ballistic (i.e., $\kappa \sim L$) to diffusive (i.e., $\kappa = $ constant). Thus, a length dependence of κ must be measured to directly obtain l. Here we present three different experimental methods to measure the length dependence of κ of the Si-Ge core-shell nanowires.

First, we employed microscale thermal conductivity test fixtures consisting of suspended SiN$_x$ pads with integrated Pt film resistors that served as independent heaters, as shown in Fig. 2. Nanowires with chosen lengths or diameters were picked up and placed on the test fixture by a sharpened tungsten tip operated by a piezodriven manipulator inside a scanning electron microscope (SEM). *In situ* deposition of the Pt/C composite was then carried out to rigidly bond the nanowire to the test fixture and to reduce contact thermal resistance. During the experiment, a constant power (P) was supplied to the heater, and the temperature rise of the heater was measured before (ΔT_b) and after (ΔT_a) connecting the nanowire. Because the thermal conductance of the tungsten tip is $\sim 10^4$ higher than the nanowire, it functions like a heat sink for the system. The thermal conductance (K) of the nanowire can be obtained via

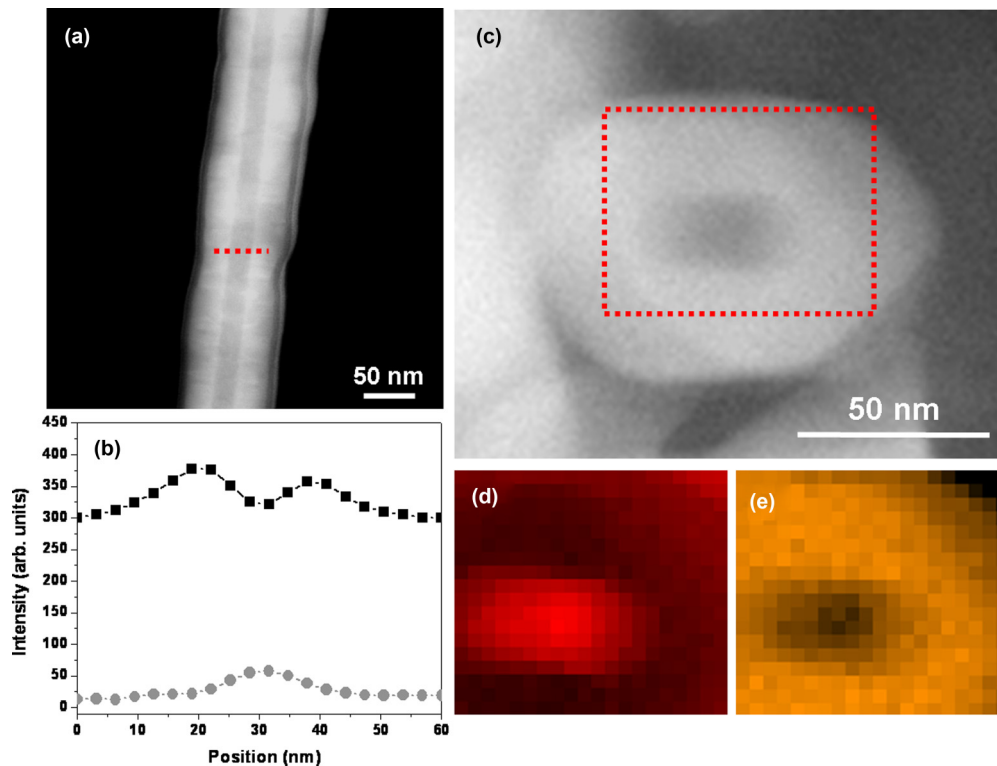$$K = P\left(\frac{1}{\Delta T_a} - \frac{1}{\Delta T_b}\right). \tag{2}$$

FIG. 1. (Color online) (a) A representative HAADF image of a Si-Ge core-shell nanowire. (b) The intensity profiles of Si K edge (gray line) and Ge K edge (black line) extracted from STEM-EDS spectra on the nanowire with the electron probe scanned across the nanowire [red dotted line in (a)]. (c) The cross-sectional HAADF image of the nanowire. The corresponding (d) Si K-edge and (e) Ge K-edge elemental maps acquired from the red rectangle area in (c) confirm the Si-core and Ge-shell structure of the nanowire.
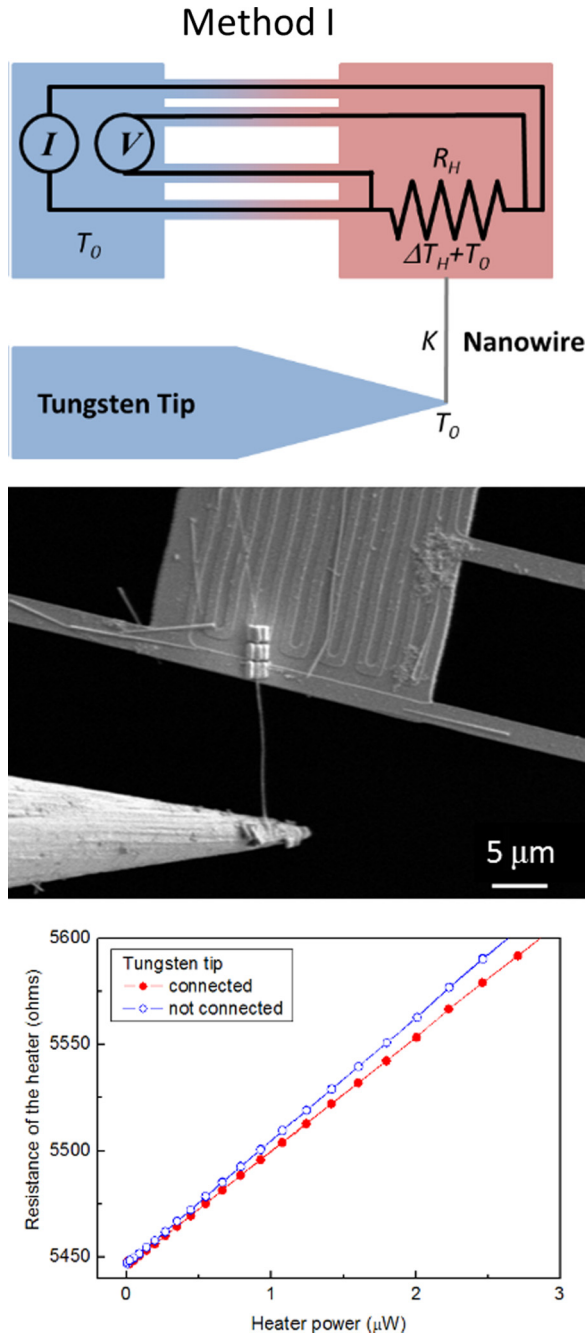
Method I

FIG. 2. (Color online) Schematics (upper) and the corresponding SEM image (middle) for Method I. Here one end of a nanowire is anchored to a microfabricated heater, and the other end is attached to a tungsten tip serving as a heat sink. The heat sink is maintained at temperature T_0, and the Joule heating raises the temperature of the heater to $\Delta T_H + T_0$. The difference of ΔT_H before and after connecting the nanowire is measured so as to determine the thermal conductance (K) of the sample. (Bottom panel) Heater resistance vs heater power of a nanowire measured using Method I. The raw data are plotted when a tungsten tip is very close to the nanowire (open blue circles) and after connecting it to the nanowire (solid red circles).

The thermal conductivity κ was evaluated by incorporating the length (L) and the diameter (d) of the nanowire, determined by SEM. After the measurement, the test fixture can be

transferred to a TEM, thus, all structural/elemental information of the measured nanowires can be obtained. As an example, the bottom panel of Fig. 2 displays the resistance of the heater when increasing the heater power. When a tungsten tip is close but not connected to the nanowire, the heat loss mainly flows through the suspended leg of the heater, with minor thermal radiation loss going through the tungsten tip. The measured background thermal conductance is 9.9×10^{-8} ($\pm 2.4 \times 10^{-10}$) W/K, from Fig. 2. After the tungsten tip is connected to the nanowire, there is additional heat loss flowing through the nanowire to the tungsten tip, and the total thermal conductance becomes 1.06×10^{-7} ($\pm 2.6 \times 10^{-10}$) W/K. Because the measured nanowire has length 9.3 μm and diameter 109 nm, the thermal conductivity of the nanowire is 6.74 ± 0.14 W/m-K. Similarly, the κs of more than 20 samples of different diameters, lengths, and structures were obtained using this method (open symbols in Fig. 7).

C. Method II

Second, the κ vs L relation was deliberately investigated on the same nanowire by repeatedly connecting/disconnecting a tungsten tip to different positions of a nanowire so as to vary the investigated L, as shown in Fig. 3. The method will reduce the data variations inherent in 20 different samples investigated by the first method. Although the method is elaborative and difficult, we have successfully obtained one set of data (solid green stars in Fig. 7).

It should be noted that for Method I and Method II, the resolution is much better than previous experiments employing independent suspended heater and sensor [22,23]. The improved sensitivity is mainly due to Eq. (2). That is, the thermal conductance (K) of the nanowire is obtained by measuring the temperature rise of the heater (ΔT_h) before and after connecting to the tungsten tip. From Eq. (2), the uncertainty (δx) of a measured quantity x can be written as

$$\frac{\delta K}{K} = \frac{\delta P}{P} + \frac{\delta(\Delta T_h)}{\Delta T_h}. \tag{3}$$

For comparison, the uncertainty of the previous experiments employing independent heater/sensor obeys the following relation [23]:

$$\frac{\delta K}{K} = \frac{\delta P}{P} + \frac{\delta(\Delta T_s)}{\Delta T_s} + 2\frac{\delta(\Delta T_h)}{\Delta T_h}, \tag{4}$$

where ΔT_s is the temperature rise of the sensor. Because $\Delta T_h \gg \Delta T_s$, $\delta(\Delta T_h) \sim \delta(\Delta T_s)$, and $\delta P/P \sim \delta(\Delta T_h)/\Delta T_h$, we see that $\delta K/K$ is dominated by the second term in Eq. (4), whereas it is much smaller in Eq. (3). This is why we can easily achieve $\sim$0.25 nW/K resolution in thermal conductance measurements using Method I without incorporating balanced bridges or lock-in techniques [24,25].

D. Method III

For Method III, we employed an electron-beam-heating technique similar to the method developed by D. Liu *et al.* [26]. As shown in Fig. 4, we fabricated a thermal conductivity test fixture consisting of two integrated Pt film resistors supported
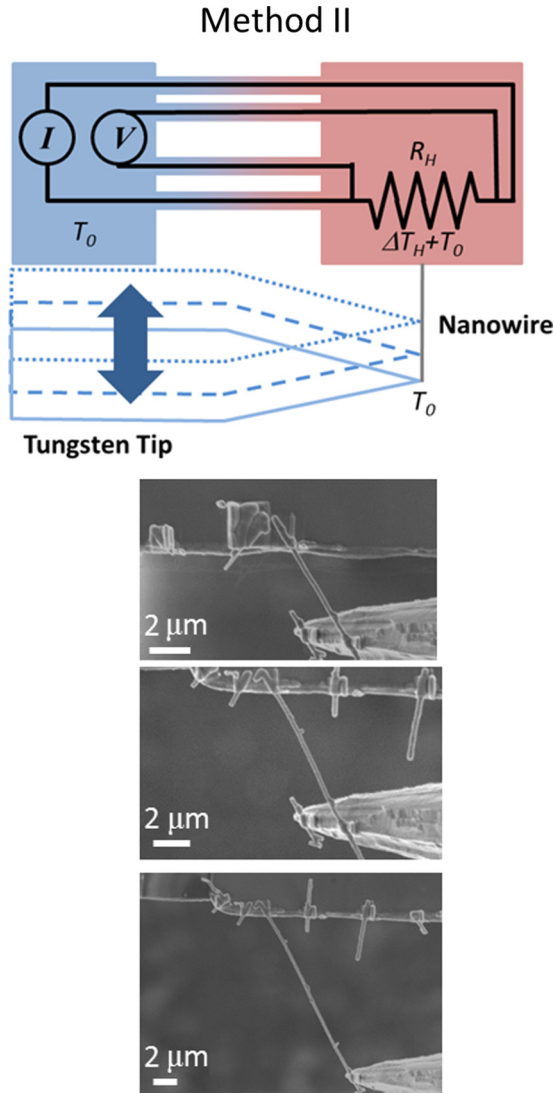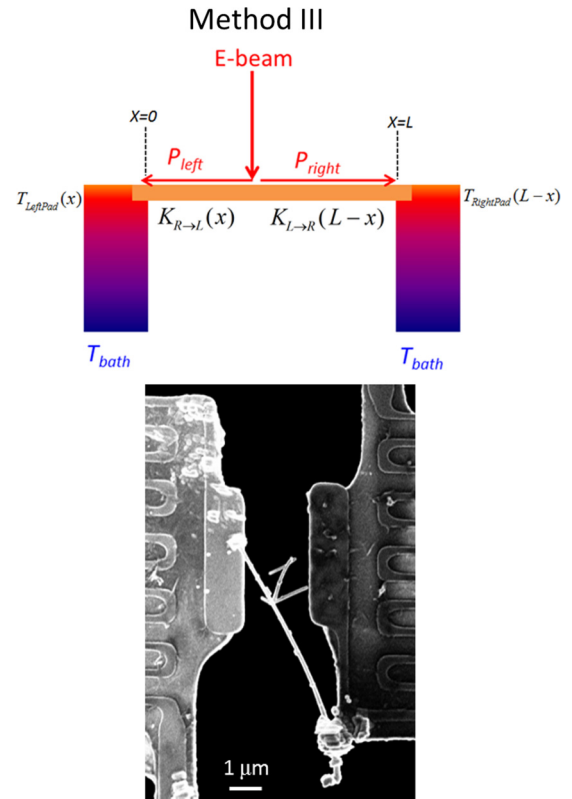
Method II

Method III

FIG. 4. (Color online) Schematics (upper) and the corresponding SEM image (lower) for Method III. Here a nanowire is anchored between two suspended sensors, and an electron beam is focused on the nanowire serving as a local heater. Interestingly, the two dangling short nanowires attached to the long nanowire shown in the SEM image do not affect the measurement result.

obtained using the relation

$$
K_{\text{total}} = \frac{1}{R_{NW} + R_{c,\text{left}} + R_{c,\text{right}}}
$$
$$
= \frac{P}{\Delta T_h - \Delta T_s} \left(\frac{\Delta T_h}{\Delta T_h + \Delta T_s} \right). \tag{5}
$$

By switching the role of heater and sensor, we can respectively determine the thermal conductance for heat flux flowing from right to left ($K_{R \to L}$) and left to right ($K_{L \to R}$).

We then employed an electron beam (5 kV) of SEM and focused at position x of the nanowire ($x = 0$ is located at the edge of the left pad). Due to electron-phonon inelastic scatterings, the electron beam acted as a local heater generating total power $P_{\text{total}}(x)$ and raised the local temperature at position x to $T(x)$. Under steady state, we have the following relation:

FIG. 3. (Color online) Schematics (upper) and the corresponding SEM images (lower) for Method II. Similar to Method I, but now the tungsten tip can repeatedly connect/disconnect to the nanowire so as to vary the investigated L.

by suspended SiN$_x$ pads. The Pt film resistors also served as independent heaters and sensors for measuring the Joule heating power (P) and temperature variations (ΔT_h and ΔT_s). Under steady state, the total thermal conductance (K_{total}) of the system [including contributions from the thermal resistance of the nanowire (R_{NW}) and the (classical) contact thermal resistances at the left/right pads ($R_{c,\text{left}}$ and $R_{c,\text{right}}$)], can be

$$
\begin{aligned}
P_{\text{total}}(x) &= P_{\text{left}}(x) + P_{\text{right}}(L - x) \\
P_{\text{left}}(x) &= K_{R \to L}(x)(T(x) - T_{\text{LeftPad}}(x)) = K_{\text{LeftPad}}(T_{\text{LeftPad}}(x) - T_{\text{bath}}) \\
P_{\text{right}}(L - x) &= K_{L \to R}(L - x)(T(x) - T_{\text{RightPad}}(L - x)) = K_{\text{RightPad}}(T_{\text{RightPad}}(L - x) - T_{\text{bath}})
\end{aligned}, \tag{6}
$$

where $P_{\text{left}}(x)$ and $P_{\text{right}}(L - x)$ are, respectively, the heat flux flowing to the left and to the right pads when the electron beam is positioned at x. $K_{R \to L}(x)$ and $K_{L \to R}(L - x)$ are the thermal

conductance of the nanowire measured at distances x and $L - x$ for heat flux flowing from right to left and left to right, respectively. $T_{\text{LeftPad}}(x)$, $T_{\text{RightPad}}(x)$, and T_{bath} denote the

temperature measured at the left pad, the right pad, and the heat bath, respectively. The unknowns in Eq. (6) are, respectively, $T(x)$, $K_{R\to L}(x)$, and $K_{L\to R}(L-x)$.

Because $T(x)$ is determined by the inelastic electron-phonon scatterings, here we assume $T(x)$ is proportional to $P_{total}(x)$ such that $T(x)$ can be obtained if $K(x')$ at position x' is determined. Experimentally, it can be done by positioning the electron beam at $x = -\varepsilon$, $L + \varepsilon$, ($\varepsilon < 1\,\mu$m), which is equivalent to heating the left pad and the right pad, respectively. Correspondingly, $K_{L\to R}(L+\varepsilon)$ and $K_{R\to L}(L+\varepsilon)$ can be independently determined by the thermal conductivity test fixture; thus, we can obtain $T(-\varepsilon)$ and $T(L+\varepsilon)$ [note that $T(-\varepsilon)$ and $T(L+\varepsilon)$ are local temperatures at the ends of the nanowire anchored on the pads but not the temperature of the pads]. Therefore, unlike the previous report where diffusive thermal conduction was presumed in the analyses [26], our method is capable of probing ballistic thermal conduction of a nanowire.

Experimentally, we employed the spot function of the SEM to focus the electron beam at various positions of a nanowire. A homemade electrode was attached to the pole piece of an SEM to modulate the electron beam, as shown in Figs. 5(a) and 5(b). The modulation frequency was set at 2 Hz, and the modulation amplitude was adjusted to be ∼50% larger than the diameter of the nanowire. The resistance variations of the two sensors were simultaneously measured as a function of time using two Stanford 830 lock-in amplifiers and two Keithley 220 current sources supplying dc currents $1 \sim 2\,\mu$A. Because the electron beam irradiated and heated up the nanowire twice during each oscillation, we locked the frequency at 4 Hz. As shown in
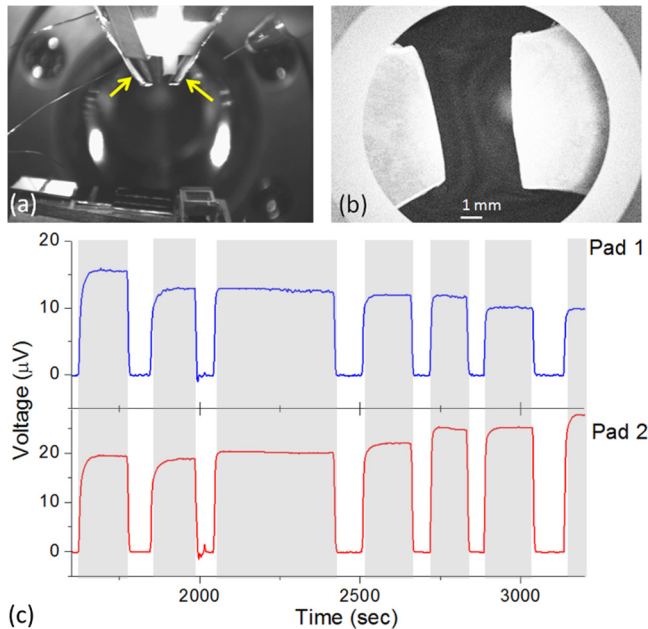

(c)

FIG. 5. (Color online) (a) A homemade electrode (indicated by the yellow arrows) attached to the pole piece of an SEM for modulating the electron beam. (b) SEM image of the electrode. (c) Voltage variations of the two sensing pads when an electron beam scans in a zigzag path gradually leaving pad 1 and moving toward pad 2. The gray (white) areas denote when the electron beam irradiates the nanowire (blank regions).

Fig. 5(c), when the electron beam irradiates at the nanowire, the temperatures at the two sensing pads increase substantially, resulting in the voltage increases measured by the lock-in amplifiers. Background contributions due to backscattering of high energy electrons from the sample holder were measured by focusing the electron beam at a nearby blank region and were found to be negligibly small. Figure 5(c) shows the signal variations when the electron beam is moved in a zigzag path, gradually leaving pad 1 and moving toward pad 2. It can be seen that during the process, the signals of pad 1 decrease while those of pad 2 increase. In addition, Fig. 5(c) shows strong stabilities of the signal, which demonstrates that prolonged electron irradiation does not affect the thermal transport properties of the nanowire.

We have repeated the process shown in Fig. 5(c), and the two sets of data [i.e., $\kappa(x)$ and $\kappa(L-x)$] are shown in Fig. 7 (red and blue solid symbols). The (classical) contact thermal resistances are obtained by comparing the thermal resistances at $x = \pm\varepsilon$ and $L \pm \varepsilon$. We obtain $R_{c,\mathrm{left}} \sim R_{c,\mathrm{right}} < 2.1 \times 10^6$ K/W, which is consistent with the results obtained from extrapolating the length-dependent thermal resistance to $L \to 0$ in the inset of Fig. 8 (i.e., $R_{c,\mathrm{left}} \sim R_{c,\mathrm{right}} < 1.6 \times 10^6$ K/W).

E. Effects from Pt/C composites

The Pt/C composites were deposited by electron-beam-induced deposition inside an SEM chamber to anchor the nanowire on the thermal conductivity test fixtures or the tungsten tips. Figure 6 shows TEM/STEM images of several broken nanowires after we finished the experiments. We noticed that the Pt/C would diffuse along the nanowires even if we deposited the Pt/C at the contacts only. The unwanted Pt/C depositions were as thick as 20 nm near the contacts, but they became thinner than 10 nm when they were 0.5 μm away from the contacts.

The thermal conductance of the unwanted Pt/C composite ($K_{Pt/C}$) could contribute to the measured thermal conductance (K_{meas}), in addition to that of a nanowire (K_{NW}), i.e., $K_{\mathrm{meas}} = K_{NW} + K_{Pt/C}$. Given that the thermal conductivity of Pt/C composites is ∼1 W/m-K and that their thickness becomes thinner than 10 nm for $L > 0.5\,\mu$m, we estimate $K_{Pt/C} < 3.2 \times 10^{-9}$ W/K at $L = 1\,\mu$m (for a nanowire diameter ∼200 nm), which contributes less than 0.5% of the K_{meas}. Therefore, the contribution from the unwanted Pt/C composite is negligible and will not affect the ballistic thermal conduction described later in this work.

III. RESULTS

Putting all data together in Fig. 7, they clearly show strong correlation between κ and L for $L < 5\,\mu$m. According to Landauer's formulation of quantum (ballistic) conductors [27], no dissipation will occur inside a ballistic conductor, and thermal resistance only happens at the contacts, resulting in a linear L dependence of κ for $L < 5\,\mu$m. When the thermal transport becomes diffusive, additional dissipation will occur inside the nanowire, resulting in an L independence of κ for $L > 5\,\mu$m. Remarkably, Fig. 7 shows that the ballistic to diffusive transition occurs at $L \sim 5\,\mu$m, indicating $l \sim 5\,\mu$m
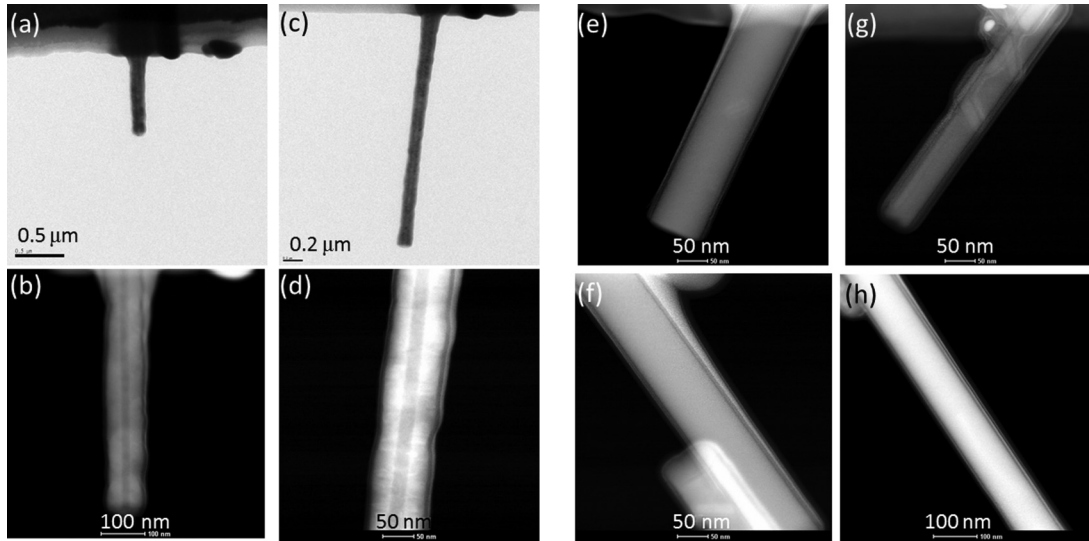
FIG. 6. TEM/STEM characterizations of Pt/C diffusion along the nanowires. (a), (c) TEM images of two different Si-Ge core-shell nanowires. (b), (d) Corresponding STEM images. (e)–(h) STEM images of four different SiGe homogeneously alloyed nanowires reported previously in Ref. [9]. The outermost amorphous layer indicates that the Pt/C composites are as thick as 20 nm near the contacts, but they became thinner than 10 nm when they are 0.5 μm away from the contacts. Because the tungsten tip needs to be disconnected from the nanowire after finishing the experiment, the disconnecting process often cleaves the nanowire, thus the lengths shown here are considerably shorter than the original ones.

for the Si-Ge core-shell nanowires. Controlled experiments on Si nanowires indeed display the expected diffusive transport behavior, confirming the validity of our experiments (see the Appendix). The results of Si-Ge core-shell nanowires not only largely deviate from the indirect estimates that $l < 100$ nm for SiGe alloys [14,28–31], but they are also much longer than $l \sim 1\,\mu$m proposed for the best thermal conductors like diamond and graphene [1]. The finding also highlights the impor-
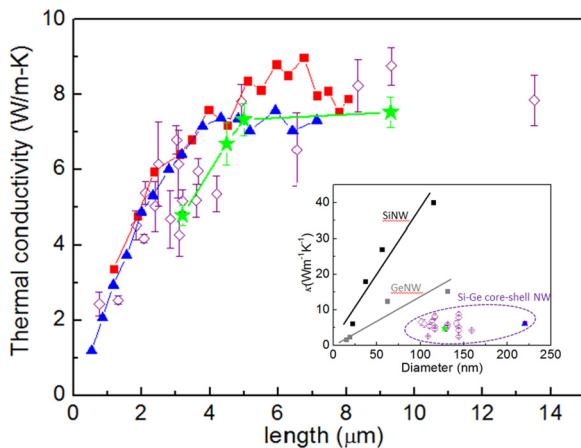

FIG. 7. (Color online) κ vs L determined by three independent experimental methods. Method I (open diamonds) determines κ vs L for 20 Si-Ge core-shell nanowires of different lengths, diameters, and structures. Method II gives one set of data (green solid stars). Method III contributes two sets of data (red and blue solid symbols, here the error bars are compatible to the size of the symbols). (Inset) κ vs d relation for the investigated nanowires (data circled by the dashed line), Si nanowires (black squares) and Ge nanowires (gray squares).

tance of our direct, rigorous, thermal transport measurements on l.

In contrast, κ displays much weaker dependence on the diameter (d), as shown in the inset of Fig. 7. For comparison, we find that the normalized variation ($\Delta\kappa/(\kappa_{\text{bulk}}\Delta d)$, where $\Delta\kappa/\Delta d$ is the slope of the linear fit, κ_{bulk} is the bulk value of κ, $\kappa_{\text{bulk}} = 150$ W/m-K for Si, $\kappa_{\text{bulk}} = 58$ W/m-K for Ge) is 2.3×10^{-3}/nm for Si nanowires and 2.2×10^{-3}/nm for Ge nanowires [18,32–34], whereas $\Delta\kappa/(\kappa_{\text{bulk}}d) < 3 \times 10^{-4}$/nm for Si-Ge core-shell nanowires for $d = 100 \sim 220$ nm (here κ is also a function of L and must be incorporated for the analyses). Because surface roughness is known to scatter high-frequency phonons [35], the much weaker d dependence of κ in Si-Ge core-shell nanowires indicates the absence of high-frequency phonons in carrying out the heat conduction.

Classically, the thermal conduction of scattering-free phonons is unlimited, and thus perfect phonon transmission would indicate zero (classical) contact thermal resistance. Quantum mechanically, however, Landauer's formulation dictates that each ballistic quantum channel exhibits finite thermal conductance, and the (quantum) contact thermal resistance always occur whenever phonons are squeezed into a narrow channel from a heat bath. Note that the two contact thermal resistances are characteristically different in nature; the former arises from phonon backscatterings, whereas the latter is mainly due to geometrical constraints of quantum channels. Remarkably, we have observed the distinct contact thermal resistances in Fig. 8. Note that the data for $L > 5\,\mu$m can be extrapolated to zero when $L \to 0$, suggesting negligible classical contact thermal resistance. In contrast, finite quantum contact thermal resistance occurs for $L < 5\,\mu$m and remains constant even when $L \to 0$, obeying Landauer's formulation for ballistic phonons. Similar phenomena have also been
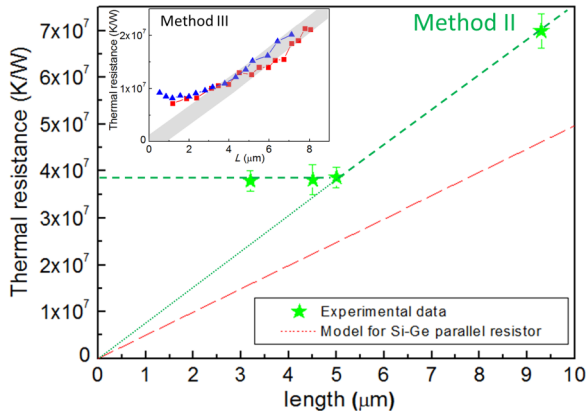
FIG. 8. (Color online) Thermal resistance vs L determined by Method II (green stars). The green dashed line is a guide to the eye. Note that the data for $L > 5\,\mu$m can be extrapolated to nearly zero when $L \to 0$ (thin dotted line). (Inset) Similar behavior (indicated by the gray belt) is also observed in another nanowire measured using Method III. The red dashed line is the calculated thermal resistance based on a parallel (diffusive) resistor model of identical geometry. Note that for $L > 5\,\mu$m, the thermal resistance of the green dashed line is 40% larger than that of the model, indicating suppressed thermal conductivity. The suppressed thermal conductivity becomes more pronounced due to the presence of ballistic phonons at $L < 5\,\mu$m.

observed in another sample measured using Method III, as shown in the inset of Fig. 8. We emphasize that these remarkable effects are observed at room temperature, whereas the corresponding electrical analogies were known to occur at ultralow temperatures only [36].

In addition to the evidence of $l \sim 5\,\mu$m in Fig. 8, the data also display suppressed κ in Si-Ge core-shell nanowires. To investigate the effect, we have calculated the thermal resistance based on a diffusive phonon model where the Si core and the Ge shell are assumed to contribute parallel to the total thermal resistance. In this model, the κs are obtained from the experimental data of Si nanowires and Ge nanowires of similar diameters so that surface scatterings have been included [18,32–34]. The thermal transport model assumes that the thermal conductances of the Si core and the Ge shell independently contribute to the total thermal conductance (K_{total}) in parallel. Thus,

$$K_{\text{total}} = \kappa_{\text{core}} \frac{\pi r_1^2}{L} + \kappa_{\text{shell}} \frac{\pi \left(r_2^2 - r_1^2\right)}{L}, \tag{7}$$

where r_1 is the radius of the Si core, r_2 is the outer radius of the Ge shell, and L is the length of the nanowire. In order to incorporate the effect of surface scatterings in the model, the thermal conductivities of the Si core (κ_{core}) and Ge shell (κ_{shell}) are respectively assigned by incorporating data of nanowires of similar radii. For the nanowire shown in Fig. 8, we assign $\kappa_{\text{core}} = 19$ W/m-K and $\kappa_{\text{shell}} = 15$ W/m-K. Note that this model ignores the added effects from the Si-Ge interface. Thus, any discrepancies between the experimental data and the model can be attributed to the heterogeneous Si-Ge interface. Figure 8 shows that in the diffusive regime ($L > 5\,\mu$m), the measured thermal resistance is 40% larger than that of the

model, indicating additional suppression on κ from the Si-Ge interface. In the ballistic regime ($L < 5\,\mu$m), the suppression of κ becomes dramatically pronounced. Notably, previous theoretical works either underestimated the l or ignored that the presence of ballistic phonon transport had given incorrect estimates on the suppressed κ [10–15].

In principle, the nature of ballistic thermal conduction can be observed either from κ vs L relation or from $1/K$ vs L relation, as shown in Fig. 8. However, because of the diameter variations of different nanowires measured using Method I, we instead plot the κ vs L relation and the normalized thermal resistance (A/K, where A is the cross-sectional area of each nanowire) vs L relation in Figs. 9(a) and 9(b).

Note that the ballistic thermal conduction becomes less evident in Fig. 9(b) even when they are plotted using the same data in Fig. 9(a). We believe that it is mainly due to the lack of universality in different samples, including different lengths of ballistic thermal conduction, structural variations, and uncertainties in the contacts that shadow the effect. To justify our explanation, we plot similar relations of Si thin films obtained by other groups [7]. As seen in Fig. 9(c), the κ vs L relation changes the slope at $L \sim 140$ nm, which has been considered as the evidence of (averaged) phonon mean free path ~140 nm for Si. However, due to the lack of universality between different samples, it is difficult to observe the effect in the corresponding A/K vs L relation in Fig. 9(d).

On the other hand, our previous work on homogeneously alloyed SiGe nanowires shows much better universality among different samples [9]. As shown in Figs. 9(e) and 9(f), both the κ vs L relation and the A/K vs L relation show clear evidence for ballistic thermal conduction over 8.3 μm. We believe that the problems associated with the A/K vs L relations shown in Figs. 9(b) and 9(d) could be due to visual effects. Nevertheless, these problems certainly raise concerns on the validity of the evidence. To rigorously demonstrate the ballistic thermal conduction, it is necessary to obtain κ vs. L and $1/K$ vs. L relations on the same sample so as to minimize the unwanted experimental variations. The result highlights the importance of Method II and Method III employed in our work.

The suppressed κ in Si-Ge core-shell nanowires are further analyzed in terms of shell/core ratio [$(r_2 - r_1)/r_1$, where r_1 is the radius of the Si core, and r_2 is the outer radius of the Ge shell] in Fig. 10. Here we have employed STEM mapping to unravel the detailed structures of the investigated nanowires. Molecular dynamics simulations on much thinner nanowires have suggested phonon localization would occur at the heterogeneous interface and lead to suppressed κ via a few layers of surface coating. But the effect would cease to dominate beyond some critical coating thickness (~4 nm) [12–15]. Thus, when further increasing the Ge-coating thickness, the total κ will start to increase and may exceed the κ of the constituent Ge shell [12–15]. Interestingly, our nanowires exhibit much thicker ($r_2 - r_1 > 30$ nm) Ge coatings yet show reduced κ. Thus, the experimental result indicates that the proposed phonon localization effect may extend to much larger distances than theoretically anticipated [13–15]. Moreover, for the given $(r_2 - r_1)/r_1$ and r_1, the data in Fig. 10 show opposite trends from theoretical predictions based on Boltzmann transport equations [10,11]. That is,
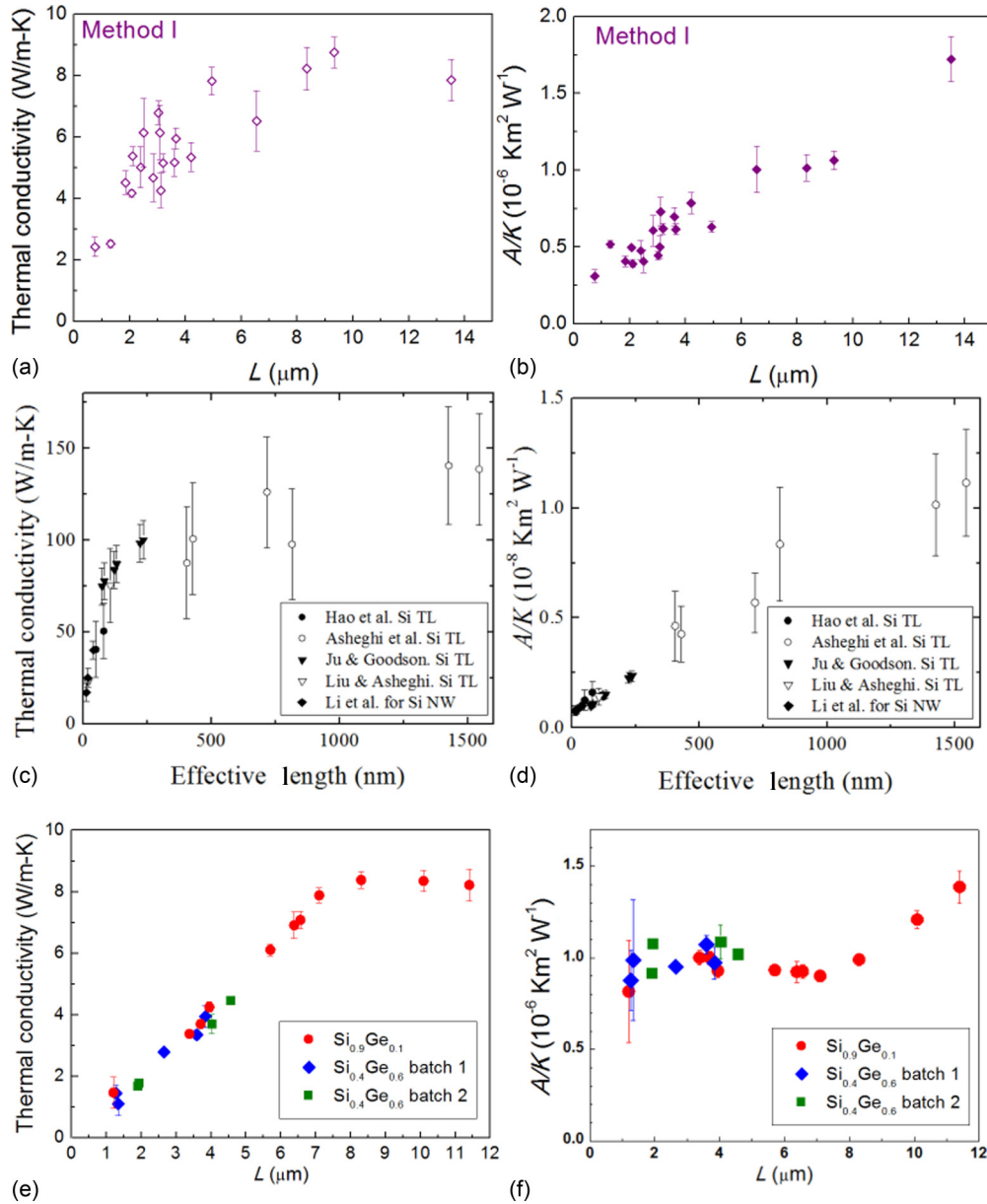
FIG. 9. (Color online) κ vs L relation (left) and A/K vs L relation (right), respectively, for (a), (b) Si-Ge core-shell nanowires measured using Method I; (c), (d) Si thin film data reproduced from Ref. [7]; and (e), (f) homogeneously alloyed SiGe nanowires from Ref. [9].

the suppression of κ is unexpectedly pronounced for large r_1. The result again indicates that the suppressed κ has extended to regions far away from the Si-Ge interface, i.e., the heterogeneous interface induces phonon filtering in the whole body of a nanowire.

To unravel the mechanism for the simultaneous elongation of l and suppression of κ, we notice that the pronounced κ vs L relations shown in Fig. 7 and Fig. 8 persist even when twin boundaries, defects, and rough surfaces are present in the nanowires. Because phonon scatterings by defects increase with $\sim\omega^4$ (where ω is phonon frequency), the phonons that carry out the heat conduction process should exhibit long wavelengths, otherwise they will not propagate inside the nanowire for ~ 5 μm. Furthermore, the weak diameter dependence of κ shown in the inset of Fig. 7 also

suggests the dominant role of low-frequency phonons in transmitting thermal energy without being scattered by surface roughness. Last, the small classical contact thermal resistance determined in our experiments is also consistent with the low-frequency phonon picture that shows insensitivities to nanoscale perturbations.

The hypothesis of low-frequency phonons mentioned above suggests that the phonon spectrum in carrying out the heat conduction is nearly monochromatic and dispersiveless. Thus we can simplify Eq. (1) to $\kappa = C_a v_a l/3$ (where C_a and v_a are the specific heat and sound velocity of the low-frequency acoustic phonons in Si-Ge core-shell nanowires, respectively). In the ballistic regime, $l = L$ and $\kappa = C_a v_a L/3$. Surprisingly, we find that the slope of the data in Fig. 3 ($\kappa/L = C_a v_a/3 \sim 2 \times 10^6$ W/K-m^2) is only 0.1% of the bulk's value
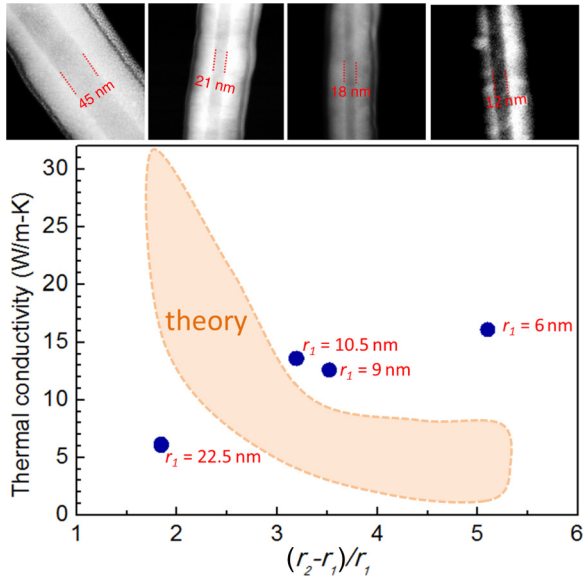
FIG. 10. (Color online) (Top figures, from left to right) STEM images of four investigated nanowires with $(r_1, r_2) =$ (22.5 nm, 64 nm), (10.5 nm, 44 nm), (9 nm, 45.5 nm), and (6 nm, 36.5 nm), respectively. The contrast is much enhanced for the farthest right image to highlight the Si core. (Bottom panel) κ vs $(r_2 - r_1)/r_1$ for the investigated nanowires and their respective r_1s. Due to the ballistic thermal conduction, here the κ data are compared at $L = 3\,\mu$m. The corresponding theoretical predictions (shaded area) for the given $(r_2 - r_1)/r_1$ and r_1 are shown for comparison (here the theoretical predictions, including specular and diffusive surface scatterings, are either interpolated or extrapolated from Fig. 3 of Ref. [10]).

$(C_{\text{bulk}} v_{\text{bulk}}/3 = 1.7 \times 10^9$ W/K-m$^2)$ [37]. Because the sound velocity determined from the bulk measurements should not deviate much from the averaged phonon velocity for the low-frequency acoustic phonons, the result indicates $C_a/C_{\text{bulk}} = 0.1\%$. That is, only 0.1% of the total excited phonons carry out the heat conduction process in the Si-Ge core-shell nanowires while the majority of the high-frequency phonons are localized. The localized modes block most heat conduction channels, resulting in a reduced κ. Applying similar analyses to Si films [6], Ge films [7], and carbon nanotubes [2] reveal that ~30% of the excited phonons are responsible for ballistic heat conduction, agreeing with previous theoretical analyses [38]. The analyses can be further justified by noting the saturated $\kappa \sim \kappa_{\text{bulk}}$ in Fig. 7 indicates $l = 3\kappa_{\text{bulk}}/C_a v_a \sim 5\,\mu$m, which is consistent with our result.

Compared with the recent discovery that $l > 8.3\,\mu$m for homogeneously alloyed bulk SiGe [9], the slightly reduced $l \sim 5\,\mu$m observed in Si-Ge core-shell nanowires could be due to the phase segregation of Si and Ge elements that makes the phonon localization less effective. Because neither Si nor Ge channels exhibit l longer than 200 nm [6,7], the pronounced elongation of l in Si-Ge core-shell nanowires must be attributed to phonons propagating along the tubular Si-Ge interfaces, with added small contributions from Si or Ge channels. Even if interlayer diffusion may cause the Si-Ge interface to be effectively thicker than theoretically anticipated, a 5% alloy

concentration set by the STEM detection limit is sufficient to induce the micron-scale ballistic thermal conduction. These findings will open new opportunities for realizing wave engineering of phonons at micron scales.

ACKNOWLEDGMENTS

APPENDIX

1. Controlled experiments on a Si nanowire (Method II)

Figure 11 shows the measured thermal resistance $(1/K)$ vs length (L) on the same Si nanowire measured using Method II. Because the investigated ls are much larger than the phonon mean free path of Si nanowire $(l_{\text{Si}} < 140$ nm) [6,32,33], the system is within the diffusive thermal conduction regime. As shown in Fig. 11, the $1/K$ vs L follows a linear relationship down to $L = 2\,\mu$m, which is consistent with the expected diffusive thermal transport behavior. In addition, the extrapolated line gives a nonzero offset at $L = 0$, indicating finite contact thermal resistance. From the slope and the offset, we determine $1/K = 7.4 \times 10^7$ K/W for a 1-μm-long Si nanowire, and the contact thermal resistance is 1.8×10^8 K/W. The measured Si nanowire has a diameter 47 nm, and the thermal conductivity is ~6.1 W/m-K.

Compared with the reported data that showed contact thermal resistance 5×10^6 K/W and thermal conductivity ~ 18 W/m-K for a 47-nm-diameter Si nanowire [22,32], the large contact resistance and the reduced thermal conductivity observed in Fig. 11 are likely due to surface oxidation. A thick SiO$_2$ layer would make the contact resistance large and reduce the overall thermal conductivity of the Si nanowire, leading to the observed results.
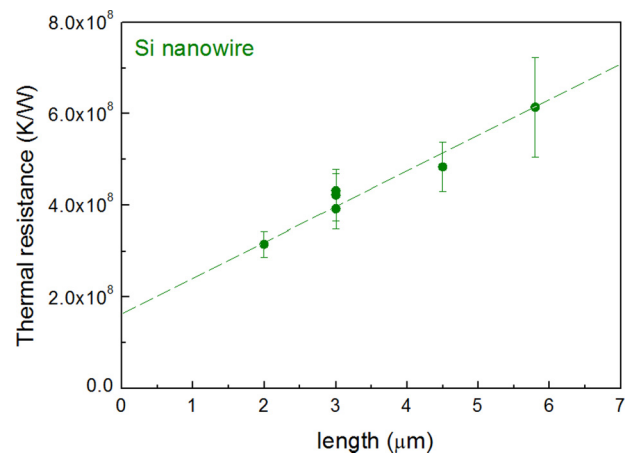

FIG. 11. (Color online) $1/K$ vs L relation investigated on the same Si nanowire using Method II. Note that $1/K$ vs L follows a linear relationship down to $L = 2\,\mu$m and gives a nonzero contact thermal resistance at $L = 0$.

[1] A. A. Balandin, Nat. Mater. **10**, 569 (2011).

[2] H. Y. Chiu, V. V. Deshpande, H. W. C. Postma, C. N. Lau, C. Miko, L. Forro, and M. Bockrath, Phys. Rev. Lett. **95**, 226101 (2005).

[3] A. J. Minnich, J. A. Johnson, A. J. Schmidt, K. Esfarjani, M. S. Dresselhaus, K. A. Nelson, and G. Chen, Phys. Rev. Lett. **107**, 095901 (2011).

[4] J. A. Johnson, A. A. Maznev, J. Cuffe, J. K. Eliason, A. J. Minnich, T. Kehoe, C. M. S. Torres, G. Chen, and K. A. Nelson, Phys. Rev. Lett. **110**, 025901 (2013).

[5] K. T. Regner, D. P. Sellan, Z. Su, C. H. Amon, A. J. McGaughey, and J. A. Malen, Nat. Commu. **4**, 1640 (2013).

[6] Y. S. Ju and K. E. Goodson, Appl. Phys. Lett. **74**, 3005 (1999).

[7] J. Alvarez-Quintana, J. Rodriguez-Viejo, F. X. Alvarez, and D. Jou, Int. J. Heat Mass Tran. **54**, 1959 (2011).

[8] C. Bera, N. Mingo, and S. Volz, Phys. Rev. Lett. **104**, 115502 (2010).

[9] T. K. Hsiao, H. K. Chang, S. C. Liou, M. W. Chu, S. C. Lee, and C. W. Chang, Nature Nanotech. **8**, 534 (2013).

[10] R. G. Yang, G. Chen, and M. S. Dresselhaus, Nano Lett. **5**, 1111 (2005).

[11] R. Prasher, Appl. Phys. Lett. **89**, 063121 (2006).

[12] T. Markussen, A.-P. Jauho, and M. Brandbyge, Phys. Rev. Lett. **103**, 055502 (2009).

[13] M. Hu, K. P. Giapis, J. V. Goicochea, X. L. Zhang, and D. Poulikakos, Nano Lett. **11**, 618 (2011).

[14] M. Hu, X. L. Zhang, K. P. Giapis, and D. Poulikakos, Phys. Rev. B **84**, 085442 (2011).

[15] J. Chen, G. Zhang, and B. W. Li, Nano Lett. **12**, 2826 (2012).

[16] L. Yin, E. K. Lee, J. W. Lee, D. Whang, B. L. Choi, and C. Yu, Appl. Phys. Lett. **101**, 043114 (2012).

[17] E. K. Lee, L. Yin, Y. Lee, J. W. Lee, S. J. Lee, J. Lee, S. N. Cha, D. Whang, G. S. Hwang, K. Hippalgaonkar, A. Majumdar, C. Yu, B. L. Choi, J. M. Kim, and K. Kim, Nano Lett. **12**, 2918 (2012).

[18] M. C. Wingert, Z. C. Y. Chen, E. Dechaumphai, J. Moon, J.-H. Kim, J. Xiang, and R. Chen, Nano Lett. **11**, 5507 (2011).

[19] H. Kim, I. Kim, H. J. Choi, and W. Kim, Appl. Phys. Lett. **96**, 233106 (2010).

[20] H.-K. Chang and S.-C. Lee, Appl. Phys. Lett. **97**, 251912 (2010).

[21] H. K. Chang and S. C. Lee, Nanoscale Res. Lett. **7**, 155 (2012).

[22] J. W. Lim, K. Hippalgaonkar, S. C. Andrews, A. Majumdar, and P. D. Yang, Nano Lett. **12**, 2475 (2012).

[23] L. Shi, D. Y. Li, C. H. Yu, W. Y. Jang, D. Kim, Z. Yao, P. Kim, and A. Majumdar, J. Heat. Transfer. **125**, 881 (2003).

[24] M. C. Wingert, Z. C. Y. Chen, S. Kwon, J. Xiang, and R. K. Chen, Rev. Sci. Instru. **83**, 024901 (2012).

[25] J. L. Zheng, M. C. Wingert, E. Dechaumphai, and R. K. Chen, Rev. Sci. Instru. **84**, 114901 (2013).

[26] D. Liu, R. G. Xie, N. Yang, B. W. Li, and J. T. L. Thong, Nano Lett. **14**, 806 (2014).

[27] L. G. C. Rego and G. Kirczenow, Phys. Rev. Lett. **81**, 232 (1998).

[28] M. C. Steele and F. D. Rosi, J. Appl. Phys. **29**, 1517 (1958).

[29] G. A. Slack and M. A. Hussain, J. Appl. Phys. **70**, 2694 (1991).

[30] C.-K. Liu, C.-K. Yu, H.-C. Chien, S.-L. Kuo, C.-Y. Hsu, M.-J. Dai, G.-L. Luo, S.-C. Huang, and M.-J. Huang, J. Appl. Phys. **104**, 114301 (2008).

[31] A. J. Minnich, H. Lee, X. W. Wang, G. Joshi, M. S. Dresselhaus, Z. F. Ren, G. Chen, and D. Vashaee, Phys. Rev. B **80**, 155327 (2009).

[32] D. Y. Li, Y. Y. Wu, P. Kim, L. Shi, P. D. Yang, and A. Majumdar, Appl. Phys. Lett. **83**, 2934 (2003).

[33] R. K. Chen, A. I. Hochbaum, P. Murphy, J. Moore, P. D. Yang, and A. Majumdar, Phys. Rev. Lett. **101**, 105501 (2008).

[34] A. I. Hochbaum, R. K. Chen, R. D. Delgado, W. J. Liang, E. C. Garnett, M. Najarian, A. Majumdar, and P. D. Yang, Nature **451**, 163 (2008).

[35] P. Martin, Z. Aksamija, E. Pop, and U. Ravaioli, Phys. Rev. Lett. **102**, 125503 (2009).

[36] C. G. Smith, Rep. Prog. Phys. **59**, 235 (1996).

[37] H. R. Meddins and J. E. Parrott, J. Phys. C Solid State **9**, 1263 (1976).

[38] J. Garg, N. Bonini, B. Kozinsky, and N. Marzari, Phys. Rev. Lett. **106**, 045901 (2011).